Molecular, Dynamic, and Structural Origin of Inhomogeneous Magnetization Transfer (ihMT) in Lipid Membrane

Scott D. Swanson[1], Dariya E. Malyarenko[1], Mario L. Fabiilli[1], Robert C. Welsh[1], Jon-Fredrik Nielsen[2], and Ashok Srinivasan[1]

1. Department of Radiology, The University of Michigan, Ann Arbor, MI 48109
2. Department of Biomedical Engineering, The University of Michigan, Ann Arbor, MI 48109

Corresponding Author:
Scott D. Swanson, PhD
Department of Radiology
The University of Michigan
3208A Medical Science I
Ann Arbor, MI 48109-5030

Running Title: Origin of ihMT Contrast

Word count: 5360~~0~~0, increased to address Reviewer comments.

Abstract:

Purpose: To elucidate the dynamic, structural, and molecular properties that create inhomogeneous magnetization transfer (ihMT) contrast ~~*in vivo* and in model systems~~.

Methods: ~~Human MT/ihMT imaging was performed at 3T~~. Amphiphilic lipids, lamellar phospholipids with cholesterol, and bovine spinal cord (BSC) specimens were examined along with non-lipid systems. MT, enhanced MT (eMT, obtained with dual frequency RF saturation)~~(eMT)~~, ihMT (MT – eMT), and dipolar relaxation, T_{1D}, were measured at 2.0 and 11.7 T.

Results: ~~Higher specificity is observed for ihMTR (ihMT ratio) compared to MT ratio (MTR) for white matter in humans.~~ The amplitude of ihMTR is positively correlated with T_{1D} values. Both ihMTR and T_{1D} increase with increasing temperature in BSC white matter and in phospholipids, and decrease with temperature in other lipids. Changes in ihMTR with temperature arise primarily from alterations in MT rather than eMT. Spectral width of MT, eMT, and ihMT increases with increasing carbon chain length.

Conclusions:. Concerted motions of phospholipids in white matter decrease proton spin diffusion leading to increased proton T_{1D} times and increased ihMT amplitudes, consistent with decoupling of Zeeman and dipolar spin reservoirs. Molecular specificity and dynamic sensitivity of ihMT contrast make it a suitable candidate for probing myelin membrane disorders.

Keywords: magnetization transfer, myelin membrane, white matter, lipid dynamics

Introduction

Magnetization transfer (MT) between water and immobilized molecules *in vivo* alters image contrast in MRI and provides a method to indirectly image the semisolid components in tissue (1-4). MT partially saturates the longitudinal, or Zeeman, magnetization of the semisolid spin system and transfers this depletion to water protons by chemical, proton, or magnetic exchange (5). For clinical research, MR images are typically acquired with and without RF saturation and a computed MT ratio (MTR) image is generated. More comprehensive studies provide quantitative estimates of the concentration of semisolid components in tissue (4), which has been histologically correlated to myelin content (6,7).

For many tissues, the semisolid resonance is homogeneously broadened by fast and efficient intra- and intermolecular spin diffusion mediated by strong magnetic dipolar coupling (8,9). Hence, RF saturation either with positive or with negative off-resonance affects all semisolid protons equally. Model MT systems such as gelatin, cross-linked bovine serum albumin (BSA) and agarose show this behavior, where a more rigid structure and variable proton-proton distances create a homogeneously broadened semisolid spectrum with Gaussian shape. Motions and structure of neuronal tissue, specifically myelin, are different. Fast rotation of lipid chains about the lipid director axis reduces intramolecular dipolar interactions and molecular chain diffusion removes intermolecular dipolar terms (10-12). The proton-proton distances in lipids are more uniform than those in proteins and are dominated by the 1.78 Å spacing of methylene CH_2 protons, creating a maximum rigid-lattice dipolar coupling of 21.28 kHz (splitting of 31.9 kHz). This coupling is reduced by molecular motion within the lipid membrane, characterized by an order parameter between 0 and 1 (13-15).

Furthermore, protein content in neuronal ~~lipids~~ tissues varies widely: 30% in myelin and 55% in gray matter (16). Due to the dynamic and structural aspects of neuronal lipids, ~~more~~ inhomogeneous broadening is expected to be more pronounced in protein-depleted white matter than in protein-rich gray matter.

The combination of phospholipids, sterols and proteins in neuronal tissues (16,17) create the well-known lipid bilayer system. Synthetic phospholipid membranes systems are easily fabricated and widely utilized as surrogate models of *in vivo* membranes. ~~The combination of phospholipids, sterols and proteins in neuronal tissues (16,17) create the well known lipid bilayer system.~~ NMR studies of model phospholipid systems (18-21) implicate cholesterol and galacto-

cerebrosides as specific molecular conduits for cross-relaxation and generation of MT. Solid-state NMR studies of biological membranes (22,23) reveal distinct anisotropy (orientation dependence) of the proton-proton dipolar interaction and corresponding inhomogeneous broadening of the proton semisolid resonance (24).

Recent studies have shown that applying dual-sided RF saturation at both positive and negative off-resonance frequencies generates an enhanced magnetization transfer (eMT) between water and inhomogeneously broadened semisolid components. The signal intensity differences between MT (single-sided RF saturation) and eMT (dual-sided RF saturation) is termed inhomogeneous magnetization transfer (ihMT = MT - eMT) and most prominently observed in myelinated tissue such as white matter (25,26). The enhanced RF saturation has been attributed to the presence of magnetization with dipolar order, which can be decoupled from the Zeeman magnetization with double-sided RF saturation (27-29). To establish a quantitative relation between measured ihMT parameters and tissue properties, optimize acquisition protocol for clinical studies, and ultimately infer specific disease mechanisms, the molecular origins of ihMT need to be characterized.

ihMT has been demonstrated *in vivo* primarily in white matter and in chemical samples with lamellar lipid structure (25,30), but no studies have yet elucidated the relationship between ihMT and molecular structure and dynamics of lipid membranes. Following Lee *et al.* (29) a brief treatment of the coupling and decoupling between dipolar and Zeeman spin system is presented for chemical systems with long proton T_{1D} times. We report here the dependency between temperature, ihMT signal amplitude, and the decay time of dipolar order, T_{1D} in tissue specimens, and in model molecular systems. We examine the magnitude and spectral width of ihMT in several lipid samples of different carbon chain lengths and different molecular inclusions (*e.g.* cholesterol). We also measure MT, eMT and T_{1D} in immobilized proteins and polysaccharides. These model systems provide molecular analogues of myelin membrane components. Changing temperature affects molecular motion in lipids and allows investigation of related changes in the values of MT, eMT, ihMT, and T_{1D}. These experiments elucidate how the molecular dynamics and structure of lipids are tied to generation of ihMT *in vivo*. In addition, we study effects of carbon chain length and presence of cholesterol on MT and ihMT in relation to membrane order parameter (12,14,15,24).

Theory

Provotorov theory under single-sided and double-sided RF saturation.

~~Application of~~ Provotov theory of RF saturation in strongly dipolar coupled spin systems helps explain the dependence of ihMT on proton T_{1D} (29,31,32). Outlined by Goldman (33), ~~further~~ developed for MT by Yeung *et al.* (27) and Morrison *et al.* (34), and applied by Lee *et al.* (29) to understand enhanced RF saturation in liquid crystals and by Varma *et al.* (35) to explain ihMT, Provotorov theory shows that a system of immobilized, dipolar coupled spins possess magnetization with both Zeeman and dipolar order. In a static magnetic field, the Zeeman and dipolar terms of the Hamiltonian commute and no energy is exchanged. Single-sided RF saturation couples the Zeeman and dipolar terms, allowing an exchange of energy between the reservoirs (36). While the RF acts to saturate the populations of spin energy levels of the semisolid component, both T_1 and T_{1D} processes act to restore magnetization to the steady-state. Dual-sided RF saturation, at both positive and negative RF frequencies, removes the coupling between Zeeman and dipolar magnetizations (25,29,33). Under dual frequency RF saturation, T_{1D} is eliminated and only T_1 processes restore magnetization to steady state. With the T_{1D} removed, RF saturation is more efficient, resulting in enhanced magnetization transfer (eMT) of the semisolid component. Therefore, the ihMT experiment is explained as a difference between coupled Zeeman and dipolar reservoirs with single-sided RF saturation (MT) and decoupled reservoirs with dual-sided RF saturation (eMT).

Coupling between Zeeman and dipolar order can be more easily appreciated and visualized if Equation 8 in Lee *et al.* (29) is solved, setting $W = W' = R_{RF}^b$ *and* $\Delta = \Delta'$ for single-sided RF saturation. Under these conditions the Zeeman and dipolar reservoirs are coupled and Zeeman longitudinal magnetization of the semisolid component at steady-state is,

$$M_b^{sat}(\Delta, \omega_1) = \frac{\omega_{loc}^2 + 2\Delta^2 R_{RF}^b T_{1D}}{\omega_{loc}^2 + 2\omega_{loc}^2 R_{RF}^b T_1 + 2\Delta^2 R_{RF}^b T_{1D}}, \quad [1]$$

where ω_{loc} is the local dipolar magnetic field, Δ is the off-resonance frequency of the RF pulse, T_1 is T_1 of the semisolid component, $R_{RF}^b = \frac{1}{2} w_1^2 \, g_b(\Delta)$ is the rate of saturation of the semisolid

protons, and $g_b(\Delta)$ is the normalized shape of the semisolid proton resonance, here assumed to be Gaussian (1).

** Figure 1 **

Similarly, setting $\Delta = -\Delta'$ for double-sided RF saturation (and assuming that RF saturation rates are equal at Δ and $-\Delta'$, valid for the symmetric dipolar Hamiltonian) decouples the dipolar reservoir from the Zeeman reservoir. The Zeeman magnetization of the semisolid component is then,

$$M_b^{sat}(\Delta, \omega_1) = \frac{1}{1 + 2R_{RF}^b T_1}. \quad [2]$$

All influence of the dipolar reservoir is removed from the saturation profile.

Figure 1a shows the results of calculating the b-spin magnetization with $\omega_{loc} = \sqrt{1/3\left(T_2^b\right)^2}, T_2^b = 12\ \mu s, \omega_1 = 2\ \pi\ 300 \frac{rad}{s}, T_1 = 0.1\ s, and\ T_{1D} = 20\ ms$. The local field, ω_{loc}, is set to the theoretical value for a Gaussian line (33). The difference between equations [1] and [2] produces an ihMT spectrum as a function of Δ. When T_{1D} is short (200 μs in Fig. 1b), terms in Eq. [1] with T_{1D} approach zero, and both single-sided and double-sided RF saturation are described by Eq. [2]. The physical consequence of this is that when T_{1D} is short, dipolar order is quickly dissipated, the resonance line is homogeneously broadened, and ihMT will be very small or zero (Fig. 1b). Conversely, long proton T_{1D} times will lead to large values of ihMT (Fig. 1a).

A fit of Provotrov theory to experimental data is shown in Figure 1C. A sample of 10% (w/w) Prolipid 161 (described below) was studied with MT and eMT pulse sequences with a steady-state RF field of $\omega_1 = 2\ \pi\ 369 \frac{rad}{s}$ from -50 to +50 kHz in 1 kHz steps. An ihMT profile was calculated as the difference between the two saturation profiles and fitted to the difference of Equations 1 and 2, yeilding the fitted parameters $T_2^b = 10.92 \pm 0.12\ \mu s, T_1 = 30.6 \pm 1.4\ ms, and\ T_{1D} = 21.2 \pm 0.6\ ms$. ω_{loc}, is set to Gausian value as before. Fig. 1C shows that Provotorov theory of RF saturation describes the salient features of ihMT for model lipid systems such as Prolipid 161.

Comment [SS1]: 2.2 Fit of Provotorv Theory to collected data

Materials and Methods

Sample Preparation:

Bovine spinal cord (BSC) was obtained from a local slaughterhouse, fixed in 10% neutral buffered formalin (Sigma-Aldrich, St. Louis, MO), and imbedded in 1.5% agarose. To measure tissue T_{1D}, 5 mm cubes of white and gray matter were dissected from this specimen and soaked in D_2O to replace exchangeable water protons. Similarly, hyaline cartilage was dissected from the femoral condyle of chicken legs obtained a local grocery store and bathed in D_2O to replace exchangeable water protons.

Type A Gelatin from porcine skin (G2500, 300 bloom, Sigma-Aldrich, St. Louis, MO) was added to H_2O at 15% w/w. Following hydration, the slurry was slowly heated in a microwave oven until melted. The hot solution was poured into 15 mL centrifuge tubes and allowed to cool and gel. Aqueous samples of 1.5% (w/w) agarose were made in a similar fashion.

Prolipid 161 (PL161), Ashland Specialty Ingredients), composed of cetearyl alcohol, behenyl alcohol, and hydroxyethyl cetearamidopropyldimonium chloride, forms a lamellar lipid bilayer when mixed with water. The wax-like PL161 and 600 mM $NiCl_2$ (to reduce T_1) were heated to 85 °C and mixed at 15% (w/w) PL161. An additional sample was made in D_2O.

Multilamellar phospholipid vesicles (MVLs) were prepared by dissolving dipalmitoyl phosphatidylcholine (DPPC) (Avanti Polar Lipids, Alabaster, AL) and cholesterol (Sigma-Aldrich, St. Louis, MO) in chloroform in a vial. A thin lipid film, obtained via evaporation of chloroform in a vacuum oven, was rehydrated with D_2O. The mixture was then vortexed to create and suspend MLVs in D_2O. The liposomes were subjected to four freeze-thaw cycles to assure minimum vesicle size. Final composition was 500 mg D_2O, 55 mg DPPC, and 35 mg cholesterol. Approximately 300 µL of product was transferred to a glass test tube for NMR study at 11.7 T. Mean particle size diameter of the DPPC:cholesterol sample (DPPC:Ch), determined by Coulter counter (Multisizer 4, Beckman Coulter), was 2.15 ± 1.75 µm. These large MLV structures hinder rotational diffusion (37) and result in negligible narrowing of the NMR resonance from vesicle rotation.

A lamellar liquid crystal (LLC) sample was made with (weight percent) sodium dodecyl sulfate (SDS) (23%), 1-decanol (12%), and D_2O (65%) as previously described (31). In short, a proper amount of SDS was dissolved in D_2O and decanol was swiftly mixed into the solution to create the LLC. The sample was vortexed, heated, subjected to several freeze thaw cycles, centrifuged, and aged one week to assure sample homogeneity.

Data Acquisition:

MR imaging in vivo: All human studies were approved by the University of Michigan Medical School Institutional Review Board and volunteers provided written, informed consent. Five healthy volunteers were scanned with a GE Discovery MR750 3T system. 3D, steady-state MT and ihMT images were acquired using a custom pulse sequence consisting of an MT module followed by an RF-spoiled, gradient-echo readout (Supporting Figure S1a). Images from a single subject are shown in Figure 2 All pulse sequences used were within FDA guidelines for radiofrequency SAR and gradient slew rate. Acquisition parameters were 240x240x8 matrix size; 1x1x5 mm^3 voxels; +/- 31.25 kHz acquisition bandwidth; TR/TE = 40/3 ms; TE; flip angle = 15°; RF spoiling implemented with 117° linear phase increment and 12π gradient spoiling in the through-slice direction. Ten second average SAR during the sequence was measured by the scanner to be 1.8 W/kg. In addition, a high-resolution spoiled gradient-recall (SPGR) image was acquired (isotropic 1mm^3 voxels) (flip angle =15°, TR/TE 12.2/5.2 ms).

Four sets of images were acquired: 1) no MT RF pulse (M_0 images), 2) with a 5-ms, Gaussian RF pulse at +10 kHz (+M_{sat} images), 3) with the RF pulse at -10kHz (-M_{sat} images), and 4) with a cosine modulated RF pulse at ± 10kHz (M_{cos} images). Peak amplitude B_1 field of the cosine modulated pulse was approximately 20 μT. Amplitude of RF at + 10 kHz and -10 kHz was reduced by $\sqrt{2}$ to keep RMS RF power for the dual-sided (cosine) and single-sided saturation pulses equal. The RMS B_1 field of the sequence was 4 μT. Each set of 4 images was acquired in 5.1 min. MTR images were computed as $100 \times (1 - M_{sat}/M_0)$, enhanced eMTR as $100 \times (1 - M_{cos}/M_0)$, and ihMTR images as $eMTR - MTR$.

The high-resolution SPGR images were segmented in gray matter, white matter, and cerebral spinal fluid in the native space of the subject using the VBM8 package in SPM8 resulting in probabilistic maps. The images used for the calculation of the MTR and ihMTR were co-registered to the same reference with a rigid body transformation in SPM8 and resampled to the spatial resolution of the SPGR (1mm^3).

MR imaging in vitro: Images of bovine spinal cord were acquired on a 2.0 T MRI system (Varian Unity/Inova) equipped with Acustar S-180 gradients. A spin-echo MRI pulse sequence was modified to include MT RF pulse train with two, independently controlled, frequencies (Fig.

Comment [SS2]: 2.1 Human Subjects deleted

2a). As above, four sets of images were acquired with no RF, (+/+) RF saturation, (-/-) RF saturation, and (+/-) RF saturation. The duration of the 5 sigma, Gaussian-shaped RF pulses was 500 μs and the pattern repeated 2000 times for each line of k-space. Peak B_1 amplitude was 20.4 μT and RMS B_1 was 10.8 μT. TR was 2.1 s and TE 11ms. Slice thickness was 5 mm and in plane resolution was 0.2 mm. Four averages were acquired and imaging time for the entire set was 84 min. Images were acquired at 20 and 40°C by changing the temperature of gradient coil cooling water. ROI contours were drawn (Matlab R2014b, The Mathworks, Natick, MA, USA) for gray matter and white matter and average and standard deviations were computed (Table 1).

*** Figure 2 ***

Single-shot MT, eMT, and ihMT of protonated model systems: Data for samples made in H_2O in 15 mL centrifuge tubes (gelatin, agarose, and PL161) were acquired at 2T with aid of a home-built, Alderman-Grant MRI probe (38). MT for all off-resonance frequencies was generated by single-shot MT spectroscopy sequence (ssMT) (39). eMT was generated by a variant of the ssMT sequence where the gradient direction is reversed to alternatively expose spins to positive and negative RF frequency offsets (Fig. 2b). A pair of 5 ms Gaussian-shaped RF pulses (peak power 18.8 μT, RMS power 10.2 μT) repeated 200 times for RF duration of 2 s. ssMT data were normalized to a 1D image with no RF saturation. ihMT was measured as the difference between regular MT, (+/+) Gz, and eMT, (+/-) Gz. Sample temperature was controlled by regulated heated air flow. MT, eMT, and ihMT in PL161 were measured as a function of temperature from 5 °C to 85 °C. MT and eMT are computed as $100 \times \left(M_{sat}^{+/+}/M_0\right)$ and $100 \times \left(M_{sat}^{+/-}/M_0\right)$, respectively. ihMT = (MT - eMT). Note that MT differs from MTR (= 100-MT), etc.

Solid-State NMR, MT Spectroscopy of Samples in D_2O: Data for samples made in D_2O were acquired in 12 mm test tubes with aid of a home-built, four-turn solenoid NMR probe tuned to 85.54 MHz. Solid-state proton NMR spectra of the model lipid samples were acquired using a 4 μs RF pulse length, 200 kHz SW. RF saturation in PL161 and LLC samples was acquired with 25 off-resonance frequencies, sampled logarithmically from 100 kHz to 100 Hz (Fig. 2c). A matrix of saturation frequencies and powers was created to enable (+/+), (-/-), and (+/-) RF saturation. Data were obtained at 20°C. The offset frequency dependence for difference spectra

of LLC and PL161 samples was measured as a function B_1 field strength. The maximum ihMT occurred at 31.0 μT for PL161 and at 1.32 μT for LLC. DPPC:Ch data were collected on an Varian 11.7T NMR (Palo Alto, CA) high-resolution NMR spectrometer.

Jeener-Broekaert Proton T_{1D} measurements of Samples in D_2O: A Jeener-Broekert sequence, $90°(\phi1) - \tau_1 - 45°(\phi2) - \tau_d - 45°(\phi3) - Acq(\phi4)$, was used to measure the decay of dipolar order (T_{1D}) (Fig. 2d). RF and receiver phase cycling over 8 acquisitions was used to eliminate multiple quantum and Zeeman order magnetization (40-42) during τ_d. As above, wide-line proton NMR spectra were typically acquired using a 4 μs RF pulse length, τ_1 of 30 μs, 100 kHz SW, 200k data points. JB data were reduced by summing the positive lobe of the dispersion-like spectrum. Data were obtained at 25 °C and 40 °C in samples of PL161, BSC white matter, and BSC gray matter exchanged with D_2O. Other data were obtained from DPPC:Ch, 10% agarose, and 15% gelatin constructed in D_2O. Fitting of the decay of dipolar order, T_{1D}, was performed with aid of the Matlab Curve Fitting Tool using the trust-region-reflective algorithm. Errors of the fitting procedure are estimated as the 95% confidence limits. Decay of dipolar order was collected on a logarithmic time scale from 1 microsecond to 1 second with 50 data points. The initial decay of magnetization is due either to fast dipolar decay, as in cartilage, or decay of the solid echo, as in Prolipid 161 and white matter. For lipid samples, decay of magnetization between 0.6 ms and 1s was used to calculate the predominately monoexponential T_{1d} decay times. ~~Following fast decay of the solid echo, dipolar order decay times were sampled exponentially between 1 ms and 1 s and found to be mono-exponential.~~

Results

~~** Figure 2 **~~

~~*In vivo* brain images obtained show higher selectivity of ihMTR contrast (Figure 2a) in white matter when compared to MTR (Fig. 2b). The ihMTR histogram illustrates a clear separation between white matter (WM) and grey matter (GM) voxels. Quantitative ROC evaluation of the WM versus GM histograms (Fig. 2c) using anatomical voxel labeling is performed for ihMTR and MTR, based on the same anatomic reference. For ihMTR, AUC is 0.69, and sensitivity and specificity are both 83%. For MTR, AUC is 0.62, sensitivity is 85% and~~

~~specificity is 73%. At the power levels and offset frequencies used here, average MTR and ihMTR in white matter are 20.9 ± 2.7 % and 5.07 ± 1.34, respectively. Finite, average ihMTR is observed in GM (2.51 ± 1.56), possibly due to cortical myelin in GM.~~

** Figure 3 **

MTR images at 20 °C Fig. 3(a-c) and 40 °C Fig. 3(d-f) for a specimen of bovine spinal cord (BSC) imbedded in agarose gel are shown in Figure 3. At 20 °C there is little difference between MTR and eMTR in either GM or WM resulting in an ihMTR 2.1 ± 0.4 for GM and 2.9 ± 0.5 for WM (Table 1). The most dramatic change in increasing the temperature to 40 °C is a drop of MTR in WM from 65.3 ± 2.2 (20 °C) to 52.4 ± 2.6 (40 °C). This drop in WM MTR causes ihMTR in WM to increase to 10.5 ± 0.7 at 40 °C. GM MTR also decreases (63.7 ±0.8 at 20°C vs. 59.7 ± 0.9 at 40 °C) leading to ihMTR for GM at 40 °C of 4.7 ± 0.9%. Agarose MT saturation is about 30%, Fig. 3(a-e), regardless of temperature or RF saturation scheme.

** Figure 4 **

Figure 4 presents the MT (= M_{sat}/M_0), eMT, and ihMT (= MT – eMT) frequency profiles (or z-spectra) for 15% w/w gelatin (Fig. 4a), 1.5% agarose (Fig. 4b) and PL161 (Fig. 4c). The sharp feature at ± 100 Hz is direct saturation of water and the broad (10-30 kHz) features are MT and eMT spectra. In gelatin and agarose (Fig. 4a,b), MT and eMT are identical and no ihMT is present (Fig. 4, Table 1). Additional studies in cross-linked bovine serum albumin (BSA) (not shown) likewise reveal zero ihMT. PL161 shows increased eMT RF saturation beyond ± 3kHz (Fig. 4c). The difference between MT and eMT is the ihMT spectrum (Fig. 4c). The ihMT effect creates up to 25% enhancement at ±12 kHz relative to regular MT in this sample and under applied experimental conditions. The ihMT spectrum forms a broad doublet slightly asymmetric toward higher frequencies.

** Figure 5 **

Temperature dependence of MT, eMT and ihMT spectra for PL161 are shown in Figure 5. Raising the temperature of the Prolipid increases the amount of regular MT (Fig. 5a) and significantly broadens the MT profile. The amount of eMT (Fig. 5b) also increases with increasing temperature, but the width of the eMT profile does not appreciably change. Comparison of Figs. 5a and 5b reveals that the spectral characteristic of the MT line shape changes more with temperature than those of the eMT line shape. Much of the ihMT temperature

dependence arises from changes in MT line shape. At 65°C (not shown) the MT becomes nearly identical to eMT. The amount of ihMT observed for PL161 (Fig. 5c) goes through a maximum near 25 °C and gradually decreases with increasing temperature, nearly vanishing at 85°C, when MT z-spectrum collapses as the lipid melts. The off-resonance frequency at which the maximum amount of ihMT increases with increasing temperature, from 10 kHz at 5 °C to 25 kHz at 55 °C (Fig. 5c). This trend is consistent with the increasing width of the regular MT spectrum with increasing temperature. In this PL161 sample, spin diffusion within the semisolid proton reservoir becomes more efficient with increasing temperature, MT and eMT become similar, and ihMT tends toward zero at higher temperatures.

** Figure 6 **

Solid NMR state spectra of PL161 in D_2O (obtained with the sequence. Fig. 2c) are shown in Figure 6. Spectra of the wide semisolid components are shown in Fig. 6a and narrow water (left) and methyl (right) components in 6b. Fig. 6a illustrates inhomogeneous RF saturation of the semisolid PL161 proton spectrum. RF applied at +10kHz (orange) preferentially saturates spins at positive offset, whereas RF applied at -10 kHz (blue) preferentially saturates spins at negative offset. Application at both positive and negative frequencies (dashed line) increases overall saturation of the PL161 protons. These same results are reflected in the MT spectra in Fig. 6b. Residual water proton magnetization (HOD) is equally reduced by either positive or negative RF (MT), but additional, enhanced MT occurs when dual sided saturation is used (Fig. 6b). Methyl protons have minimal MT because fast rotation about the three-fold symmetry axis decouples the methyl protons from the methylene protons to first order.

** Figure 7 **

Figure 7 shows synthetic dipolar spectra, generated by the difference between positive and negative RF saturation on the solid line for PL161 (Fig 7 a,c) and LLC (Fig 7 b,d) in D_2O as a function of RF frequency from ±100 Hz to ±100 kHz. The images in Figs. 7a,b and spectra in Figs. 7c,d show that PL161, with 15 to 18 carbon atoms per aliphatic chain, has a much broader spectral width and much different saturation profile than the LLC sample, composed with molecules with 10 or 12 carbon atoms. The PL 161 spectra present characteristic features of overlapping Pake patterns with peak intensities at +/-8kHz and +/-17kHz, respectively, while LLC profile peaks at ~8kHz. At large off-resonance frequencies (> 40 kHz), there is no MT and no ihMT. At small saturation frequencies (< 1 kHz), RF saturation is homogeneous. The

amplitude of the saturation RF was 31 μT for PL161 sample and 1.32 μT for the LLC sample. Though they occur at different RF amplitudes in each sample, these data are the maximum amount of ihMT obtained as a function of B_1 field strength (not shown).

** Figure 8 **

Subtraction of spectra obtained with (+/+) 10 kHz RF saturation from data obtained with (-/-) 10kHz is shown for two temperature for PL161 (Fig. 8a) and DPPC:Ch (Fig. 8b). The magnitude of the difference decreases with increasing temperature for PL161 but increases for DPPC:Ch. Fig. 8a shows that raising the temperature from 25 °C to 45 °C reduces the asymmetric RF saturation in PL161, consistent with the reduction in ihMT seen in Fig. 5 between these two temperatures. In contrast to PL161, Fig. 8b shows that increasing temperature increases asymmetric RF saturation in DPPC:Ch, consistent with the changes observed for BSC (Fig 3). Furthermore, the dipole pattern is wide, with peak frequency at about +/- 17kHz. Interestingly, the width of the PL161 saturation spectrum does not appreciably change with increasing temperature, while the integrated intensity decreases.

** Figure 9 **

Proton T_{1D} was measured for BSC white matter in D_2O and for PL161 at 25 and 40 °C and for hyaline cartilage at 25 °C. Data were fitted to a monoexponential decay. The results of fit for JB measurements, illustrated in Figure 9, clearly show that that dipolar order decays very fast in the specimen of hyaline cartilage, where protons in the protein and polysaccharide matrix are strongly coupled and homogeneously broadened. In addition dipolar order decays more slowly at 40 °C than at 25 °C for BSC white matter while the trend is reversed for PL161 with much slower decay at 25 °C versus 40 °C. These trends are consistent with temperature studies of saturation spectra summarized in Fig. 8. As outlined by Jeener and Broekaert (42) and discussed by Yang and Schleich (40), it is necessary to wait several hundred microseconds to avoid contaminating dipolar decay with decay of the proton solid echo. Even when T_{1D} times in lipids are of order 1 ms, as in white matter at 25 °C, sufficient magnetization remains at 600 μs to obtain a reasonably accurate estimate of T_{1D}.

Comment [SS3]: 2.4 Short T1d times

MTR, eMTR, and ihMTR values at (+/+) 10 and (+/-) 10 kHz of all studies are summarized in Table 1. In addition, proton T_{1D} estimates for WM, GM, gelatin, agarose, PL161, and DPPC:Ch are included. ihMT enhancement is largest in lipid-rich systems such as white matter, 25 °C PL161, and 40 °C DPPC:Ch. Proton T_{1D} values follow the same content-specific

trend and in general ihMTR is largest (above 10%) when proton T_{1D} is longest (of order 10 ms). ihMTR values presented in Table 1 are linearly correlated with measured values of proton T_{1D} (Pearson $\rho = 0.934$, $p = 7.64\ 10^{-5}$).

Discussion

These results demonstrate that ihMT is preferentially enhanced in white matter, sensitive to temperature changes, observed primarily in lipid systems, a function of lipid chain length and molecular rigidity, and intimately related to proton T_{1D}. ihMTR for all samples and temperatures are positively correlated with proton T_{1D}. We find that an ihMTR image is effectively a proton T_{1D} weighted image, where long proton T_{1D} times lead to increased ihMTR. T_{1D} is a function of both dipolar coupling strength and molecular motion occurring at the local field, ω_{loc} and is sensitive to slow motions of order kHz (43-45). These properties make ihMT contrast sensitive to the slow molecular dynamics within the myelin membrane of white matter.

As seen above, ihMT is generated when proton T_{1D} times are longer than several milliseconds. For a molecular system to have long proton T_{1D} times, three features must be present. First, there must be an *intramolecular* dipolar coupling. The inhomogeneous part of the dipolar Hamiltonian, $I_1^z I_2^z(1 - 3\cos^2\theta(t))$, cannot be averaged to zero. Second, *intermolecular* spin-spin interactions need to be decoupled by motions so that isolated systems of dipolar-coupled spins are present. If this does not occur, spin diffusion will quickly mix the two degenerate Zeeman states, as in cartilage, via the "flip-flop" term of the homonuclear dipolar Hamiltonian, $-\{I_1^+ I_2^- - I_1^- I_2^+\}(1 - 3\cos^2\theta(t))$, and cause significant homogeneous line broadening. Homogenous broadening will destroy dipolar order and suppress creation of ihMT. Finally, to generate MT, a magnetic, atomic, or molecular exchange between the semisolid component in tissue and water must exist.

ihMT imaging in BSC tissue.

BSC imaging results show that ihMTR at physiologic temperature is greater and proton T_{1D} is longer in white matter than in gray matter. These results are likely due to both the multi-lamellar structure and the relatively low protein content in myelin (30%) with respect to gray matter (55%) (16,17,46). MT in lipids occurs by proton exchange between water and exchangeable hydroxyl groups in lipids (18,21). The higher protein content of gray matter provides additional (regular) MT between water and homogenously broadened protein

components. In addition, integral membrane proteins increase lipid rigidity in annular regions near the protein (47) and create additional homogeneous broadening (48). The combination of these two aspects of protein in membranes will decrease proton T_{1D} and lessen the amount of ihMT observed in gray matter relative to white matter. The relatively high absolute MTR in GM observed for the fixed BSC sample could be related to extensive cross-linking of proteins upon formalin fixation that increases the amount of homogeneously broadened semisolid component (18,49).

MT, eMT and, ihMT images of BSC at 20 and 40 °C further support the hypothesis that changes in membrane dynamics are responsible for differences in ihMT. At 20 °C, MTR and eMTR for white matter and gray matter are similar and ihMTR is nearly zero. White matter at 40 °C, however, behaves differently. MTR decreases by 12.9% at 40 °C whereas eMTR only decreases by 5.3%. These changes show that the main sensitivity of ihMTR rests not in eMT, but in the MT signal. However, the eMT images are a critical component of the experiment, providing an image with effects of dipolar order removed and allowing computation of ihMT.

Molecular Structure, Molecular Dynamics and ihMT

Our results show that ihMT occurs in samples of PL161, in LLC and in DPPC:Ch but not in agarose or gelatin. Temperature increases in PL161 change both the intensity and frequency spread of ihMT. These findings are consistent with inhomogeneous broadening of semisolid spectra with characteristic dipole order features. These features are known sensitive functions of membrane order and fluidity determined both by membrane constitution and their dynamic regime (14,15,50).

Lipid Systems: The structure and dynamics of lipid and liquid crystal systems fulfill the criteria for inhomogeneous broadening described above. Fast motions in lipids about the lipid carbon chain partially average the intramolecular dipolar interaction and molecular diffusion eliminates intermolecular dipolar interactions (15,51). These motions give rise to the super-Lorentzian line shape in lipids, which is a projection of the CH_2 dipolar interactions onto the lipid director axis, creating broad semisolid resonance (52).

Consistent with the previous dynamic NMR results (13,53), DPPC:Ch is the most rigid of the lipids systems in this study. The structure of DPPC:Ch limits molecular rotations and translations relative to LLC and PL161, creating an environment for more efficient spin diffusion and reduced overall ihMT. PL161 is composed of amphiphilic molecules and alcohols with a

long, single carbon chains with exchangeable hydroxyl groups, whereas DPPC:Ch has two palmitoyl carbon chains at the glycerol linkage and a relatively rigid, planar cholesterol with exchangeable hydroxyl protons. This interpretation is consistent with the relative large ihMT observed in PL161 (up to 20% and greater than any other system studied here) and makes PL161 a good phantom material to test ihMT pulse sequences. However, DPPC:Ch and other phospholipid and sterol variations more accurately mimic biological membranes. Future quantitative studies of ihMT and T_{1D} as a function of membrane constituents and temperature will determine which molecular and dynamic components generate and suppress ihMT *in vivo*.

The relation between ihMT peak intensity and solid-state NMR lineshapes is further elucidated by the difference between measured dipole spectra with positive (+/+) and negative (-/-) RF saturation shown at two samples, PL161 and LLC. Higher rigidity of PL161 lipids and DPPC:Ch membranes compared to LLC results in the broader width of their saturation profiles when compared to LLC.

The ability to generate synthetic dipolar spectra is related to the length of proton T_{1D}. If T_{1D} is long, the single-sided RF saturation selectively saturates one side of the spectrum. If T_{1D} is short, spin diffusion will homogeneously couple one side to the other. The amplitude of these spectra decrease with increasing temperature for PL161 and increase for DPPC:Ch. These changes correlate with measured T_{1D} times and ihMT values. This behavior is consistent with the molecular dynamics of PL161 and DPPC:Ch existing on different sides of a T_{1D} maximum as temperature is increased. The observed dynamic changes are likely reflecting alterations in membrane structure and fluidity expected during phase transition between disordered and ordered lipid phases (50,53). Temperature effects on DPPC:Ch saturation spectra and T_{1D} times are also consistent with changes observed in BSC. In PL161 the dynamic trends are reversed, with lower ihMT and shorter proton T_{1D} times at higher temperatures. The preserved width of saturation spectra observed with increasing temperature is a likely indicator that measured dynamic T_{1D} changes are related to changes in the slow rates of molecular motion within lipid membrane.

The intensity of the ihMT signal and the frequency of the maximum ihMT also change with temperature for PL161. These findings can be explained if we assume that at room temperature there are several components which contribute to ihMT, some with small and some with large order parameters, as evident from the corresponding saturation spectra. The

components with large order parameters will be more rigid than the components with the smaller order parameters. As the temperature increases, components with the small order parameter become more fluid like and are removed from the ihMT spectrum. The components that remain are more rigid. Distance of carbon from the water bilayer interface determines the magnitude of the order parameter (13,53). Those carbons at the surface are more rigid and have a higher order parameter than those buried within the lipid bilayer.

Proteins and Polysaccharides: The semisolid proton resonance of immobilized proteins is homogeneously broadened by efficient spin diffusion (8,9) and minimal ihMT is expected. Proton T_{1D} is 1.18 ± 0.28 ms in gelatin, ~~and~~ 2.25 ± 0.67 ms for agarose, and 230.4 ± 20 µs in cartilage, similar to values reported previously in proteins (54,55) or polysaccharides (40). Lack of ihMT generation for both gelatin and agarose could possibly be explained by the relatively long, 5 ms RF pulse used in the ssMT experiment to generate MT and eMT. To test for ihMT under different experimental conditions, a cosine modulated RF pulse train with instantaneous, dual-sided RF saturation was used. These experiments also failed to generate ihMT in protein or agarose samples (results not shown). These results support the hypothesis that ihMT occurs only in spin systems with inhomogeneous broadening and long proton T_{1D} times.

In addition to lipids, other molecular systems have very long proton T_{1D} times (40) and will be amenable to coupling and decoupling of Zeeman and dipolar order by single-sided and double-sided RF saturation, respectively. It may be that there are molecular constructions *in vivo* other than white matter that generate long T_{1D} times and large ihMT signals. In principle, ihMT could be present in protein or polysaccharide systems if certain structural and dynamic conditions existed to create sufficiently long proton T_{1D} times, though we find no evidence of that here. Additional studies are needed to establish a quantitative relation between ihMT and specific tissue components.

ihMTR images appear to be sensitive to myelin content in tissue. White matter has the highest ihMTR signal and more than twice as large as in gray matter. A valid question to ask is "Is the intensity of an ihMTR image proportional to myelin?" That question remains open for investigation by quantitative ihMT studies and corresponding quantitative model fitting. The correlation between of ihMTR and myelin content remains to be established by careful histology studies.

Conclusions

This study demonstrates that ihMT contrast is defined by proton T_{1D} times in lipid and phospholipid systems, abundant in myelin membranes. A promising feature for future clinical application of ihMT imaging is that proton T_{1D} is sensitive to slow motions, of order kHz, and not seen by conventional T_1 or T_2 imaging. Alterations of slow membrane dynamics may precede changes in myelin content under certain disease processes.

Acknowledgement:

This research was supported by the United States National Center for Advancing Translational Sciences of the National Institutes of Health under Award Number UL1TR000433 and Research Funding from the Department of Radiology, University of Michigan.

References

1. Henkelman RM, Huang XM, Xiang QS, Stanisz GJ, Swanson SD, Bronskill MJ. Quantitative Interpretation of Magnetization-Transfer. Magnetic Resonance in Medicine 1993;29(6):759-766.
2. Filippi M, Campi A, Dousset V, Baratti C, Martinelli V, Canal N, Scotti G, Comi G. A Magnetization-Transfer Imaging Study of Normal-Appearing White-Matter in Multiple-Sclerosis. Neurology 1995;45(3):478-482.
3. Wolff SD, Balaban RS. Magnetization Transfer Contrast (Mtc) and Tissue Water Proton Relaxation Invivo. Magnetic Resonance in Medicine 1989;10(1):135-144.
4. Sled JG, Pike GB. Quantitative imaging of magnetization transfer exchange and relaxation properties in vivo using MRI. Magnetic Resonance in Medicine 2001;46(5):923-931.
5. van Zijl PCM, Zhou J, Mori N, Payen JF, Wilson D, Mori S. Mechanism of magnetization transfer during on-resonance water saturation. A new approach to detect mobile proteins, peptides, and lipids. Magnetic Resonance in Medicine 2003;49(3):440-449.
6. Janve VA, Zu Z, Yao S-Y, Li K, Zhang FL, Wilson KJ, Ou X, Does MD, Subramaniam S, Gochberg DF. The radial diffusivity and magnetization transfer pool size ratio are sensitive markers for demyelination in a rat model of type III multiple sclerosis (MS) lesions. Neuroimage 2013;74:298-305.
7. Turati L, Moscatelli M, Mastropietro A, Dowell NG, Zucca I, Erbetta A, Cordiglieri C, Brenna G, Bianchi B, Mantegazza R, Cercignani M, Baggi F, Minati L. In vivo quantitative magnetization transfer imaging correlates with histology during de- and remyelination in cuprizone-treated mice. Nmr Biomed 2015;28(3):327-337.
8. Akasaka K. Longitudinal Relaxation of Protons under Cross Saturation and Spin Diffusion. Journal of Magnetic Resonance 1981;45(2):337-343.
9. Kalk A, Berendsen HJC. Proton Magnetic-Relaxation and Spin Diffusion in Proteins. Journal of Magnetic Resonance 1976;24(3):343-366.
10. Wennerstrom H. Proton Nuclear Magnetic-Resonance Lineshapes in Lamellar Liquid-Crystals. Chemical Physics Letters 1973;18(1):41-44.
11. Brown MF. Deuterium Relaxation and Molecular-Dynamics in Lipid Bilayers. Journal of Magnetic Resonance 1979;35(2):203-215.
12. Brown MF, Ribeiro AA, Williams GD. New View of Lipid Bilayer Dynamics from H-2 and C-13 NMR Relaxation-Time Measurements. Proceedings of the National Academy of Sciences of the United States of America-Biological Sciences 1983;80(14):4325-4329.
13. Brown MF, Nevzorov AA. H-2-NMR in liquid crystals and membranes. Colloids and Surfaces a-Physicochemical and Engineering Aspects 1999;158(1-2):281-298.

4. Davis JH. Deuterium Magnetic-Resonance Study of the Gel and Liquid-Crystalline Phases of Dipalmitoyl Phosphatidylcholine. Biophysical Journal 1979;27(3):339-358.
5. Davis JH. The Description of Membrane Lipid Conformation, Order and Dynamics by H-2-NMR. Biochimica Et Biophysica Acta 1983;737(1):117-171.
6. Obrien JS, Sampson EL. Fatty Acid and Fatty Aldehyde Composition of Major Brain Lipids in Normal Human Gray Matter White Matter and Myelin. Journal of Lipid Research 1965;6(4):545-551.
7. Obrien JS, Sampson EL. Lipid Composition of Normal Human Brain - Gray Matter White Matter and Myelin. Journal of Lipid Research 1965;6(4):537-545.
8. Koenig SH. Cholesterol of Myelin Is the Determinant of Gray-White Contrast in Mri of Brain. Magnetic Resonance in Medicine 1991;20(2):285-291.
9. Fralix TA, Ceckler TL, Wolff SD, Simon SA, Balaban RS. Lipid Bilayer and Water Proton Magnetization Transfer - Effect of Cholesterol. Magnetic Resonance in Medicine 1991;18(1):214-223.
0. Ceckler TL, Wolff SD, Yip V, Simon SA, Balaban RS. Dynamic and Chemical Factors Affecting Water Proton Relaxation by Macromolecules. Journal of Magnetic Resonance 1992;98(3):637-645.
1. Kucharczyk W, Macdonald PM, Stanisz GJ, Henkelman RM. Relaxivity and Magnetization-Transfer of White-Matter Lipids at MR-Imaging - Importance of Cerebrosides and Ph. Radiology 1994;192(2):521-529.
2. Forbes J, Husted C, Oldfield E. High-Field, High-Resolution Proton Magic-Angle Sample-Spinning Nuclear Magnetic-Resonance Spectroscopic Studies of Gel and Liquid-Crystalline Lipid Bilayers and the Effects of Cholesterol. Journal of the American Chemical Society 1988;110(4):1059-1065.
3. Polozov IV, Gawrisch K. Characterization of the liquid-ordered state by proton MAS NMR. Biophysical Journal 2006;90(6):2051-2061.
4. Pake GE. Nuclear Resonance Absorption in Hydrated Crystals - Fine Structure of the Proton Line. Journal of Chemical Physics 1948;16(4):327-336.
5. Varma G, Duhamel G, de Bazelaire C, Alsop DC. Magnetization transfer from inhomogeneously broadened lines: A potential marker for myelin. Magnetic Resonance in Medicine 2015;73(2):614-622.
6. Girard OM, Prevost VH, Varma G, Cozzone PJ, Alsop DC, Duhamel G. Magnetization transfer from inhomogeneously broadened lines (ihMT): Experimental optimization of saturation parameters for human brain imaging at 1.5 Tesla. Magnetic Resonance in Medicine 2015;73(6):2111-2121.
7. Yeung HN, Adler RS, Swanson SD. Transient Decay of Longitudinal Magnetization in Heterogeneous Spin Systems under Selective Saturation .4. Reformulation of the Spin-Bath-Model Equations by the Redfield-Provotorov Theory. Journal of Magnetic Resonance Series A 1994;106(1):37-45.
8. Adler RS, Swanson SD, Yeung HN. A three-component model for magnetization transfer. Solution by projection-operator technique, and application to cartilage. Journal of Magnetic Resonance Series B 1996;110(1):1-8.
9. Lee J-S, Khitrin AK, Regatte RR, Jerschow A. Uniform saturation of a strongly coupled spin system by two-frequency irradiation. Journal of Chemical Physics 2011;134(23).
0. Girard OM, Prevost VH, Varma G, Cozzone PJ, Alsop DC, Duhamel G. Magnetization transfer from inhomogeneously broadened lines (ihMT): Experimental optimization of

saturation parameters for human brain imaging at 1.5 Tesla. Magnetic Resonance in Medicine 2014:n/a-n/a.

1. Lee J-S, Regatte RR, Jerschow A. Isolating chemical exchange saturation transfer contrast from magnetization transfer asymmetry under two-frequency rf irradiation. Journal of Magnetic Resonance 2012;215:56-63.
2. Provotorov BN. Magnetic Resonance Saturation in Crystals. Soviet Physics Jetp-Ussr 1962;14(5):1126-1131.
3. Goldman M. Spin temperature and nuclear magnetic resonance in solids. Oxford: Clarendon Press; 1970. ix, 246 p. p.
4. Morrison C, Stanisz G, Henkelman RM. Modeling Magnetization-Transfer for Biological-Like Systems Using a Semisolid Pool with a Super-Lorentzian Lineshape and Dipolar Reservoir. Journal of Magnetic Resonance Series B 1995;108(2):103-113.
5. Varma G, Girard OM, Prevost VH, Grant AK, Duhamel G, Alsop DC. Interpretation of magnetization transfer from inhomogeneously broadened lines (ihMT) in tissues as a dipolar order effect within motion restricted molecules. Journal of magnetic resonance (San Diego, Calif : 1997) 2015;260:67-76.
6. Clough S. Nuclear Spin Relaxation in a Rotating Tilted Reference Frame. Physical Review 1967;153(2):355-357.
7. Mackay AL, Burnell EE, Nichol CP, Weeks G, Bloom M, Valic MI. Effect of Viscosity on Width of Methylene Proton Magnetic-Resonance Line in Sonicated Phospholipid Bilayer Vesicles. Febs Letters 1978;88(1):97-100.
8. Alderman DW, Grant DM. Efficient Decoupler Coil Design Which Reduces Heating in Conductive Samples in Superconducting Spectrometers. Journal of Magnetic Resonance 1979;36(3):447-451.
9. Swanson SD. Broad-Band Excitation and Detection of Cross-Relaxation NMR-Spectra. Journal of Magnetic Resonance 1991;95(3):615-618.
0. Yang H, Schleich T. Modified Jeener Solid-Echo Pulse Sequences for the Measurement of the Proton Dipolar Spin-Lattice Relaxation-Time (T-1d) of Tissue Solid-Like Macromolecular Components. Journal of Magnetic Resonance Series B 1994;105(3):205-210.
1. Vold RL, Dickerson WH, Vold RR. Application of the Jeener-Broekaert Pulse Sequence to Molecular-Dynamics Studies in Liquid-Crystals. Journal of Magnetic Resonance 1981;43(2):213-223.
2. Jeener J, Broekaer.P. Nuclear Magnetic Resonance in Solids - Thermodynamic Effects of a Pair of RF Pulses. Physical Review 1967;157(2):232-240.
3. Resing HA. NMR Relaxation in Adamantane and Hexamethylenetetramine - Diffusion and Rotation. Molecular Crystals and Liquid Crystals 1969;9:101-132.
4. Ueda T, Takeda S, Nakamura N, Chihara H. Molecular-Motion and Phase-Changes in Long-Chain Solid Normal Alkanes as Studied by H-1 and C-13 Nmr. Bulletin of the Chemical Society of Japan 1991;64(4):1299-1304.
5. Zamar RC, Mensio O. Nuclear magnetic resonance proton dipolar order relaxation in thermotropic liquid crystals: A quantum theoretical approach. Journal of Chemical Physics 2004;121(23):11927-11941.
6. Siegel GJ, Albers RW, Brady ST, Price DL. Basic neurochemistry: molecular, cellular, and medical aspects. Burlington ; London: Elsevier Academic; 2006. xxiv, 992 p. p.

7. Lee AG. Lipid-protein interactions in biological membranes: a structural perspective. Biochimica Et Biophysica Acta-Biomembranes 2003;1612(1):1-40.
8. Simons K, Ikonen E. Functional rafts in cell membranes. Nature 1997;387(6633):569-572.
9. Koenig SH, Brown RD, Ugolini R. Magnetization Transfer in Cross-Linked Bovine Serum-Albumin Solutions at 200 Mhz - a Model for Tissue. Magnetic Resonance in Medicine 1993;29(3):311-316.
0. Redondo-Morata L, Giannotti MI, Sanz F. Influence of Cholesterol on the Phase Transition of Lipid Bilayers: A Temperature-Controlled Force Spectroscopy Study. Langmuir 2012;28(35):12851-12860.
1. Urbina JA, Moreno B, Arnold W, Taron CH, Orlean P, Oldfield E. A carbon-13 nuclear magnetic resonance spectroscopic study of inter-proton pair order parameters: A new approach to study order and dynamics in phospholipid membrane systems. Biophysical Journal 1998;75(3):1372-1383.
2. Davis JH, Auger M, Hodges RS. High resolution H-1 nuclear magnetic resonance of a transmembrane peptide. Biophysical Journal 1995;69(5):1917-1932.
3. Trouard TP, Nevzorov AA, Alam TM, Job C, Zajicek J, Brown MF. Influence of cholesterol on dynamics of dimyristoylphosphatidylcholine bilayers as studied by deuterium NMR relaxation. Journal of Chemical Physics 1999;110(17):8802-8818.
4. Gaspar R, Andrew ER, Bryant DJ, Cashell EM. Dipolar Relaxation and Slow Molecular Motions in Solid Proteins. Chemical Physics Letters 1982;86(4):327-330.
5. Danek AN, Bryant RG. Decay of dipolar order in diamagnetic and paramagnetic proteins and protein gels. Journal of Magnetic Resonance 2000;143(1):35-38.

Table1

Percent MTR, eMTR and ihMTR measured at ± 10 kHz RF saturation

Material	Temp.(°C ±1)	MTR	eMTR	ihMTR	T_{1D}(ms) [dc]
~~*In vivo* human (collected at 3.0 T) [a]~~					
~~GM~~	~~37~~	~~16.02 ± 4.89~~	~~18.54 ± 6.08~~	~~2.51 ± 1.56~~	
~~WM~~		~~20.9 ± 2.7~~	~~26.05 ± 3.67~~	~~5.07 ± 1.34~~	
BSC[ab]					
GM	20	63.7 ±0.8	65.9 ±0.8	2.1 ± 0.4	1.59 ± 0.57
WM		65.3 ± 2.2	68.2 ± 2.1	2.9 ± 0.5	2.41 ± 0.36
GM	40	59.7 ± 0.9	64.4 ± 0.7	4.7 ± 0.9	4.06 ± 1.20
WM		52.4 ± 2.6	62.9 ± 2.5	10.5 ± 0.7	11.6 ± 1.5
Samples [be] (± 0.15)					
Gelatin (15%)	22	24.0	24.3	0.07	1.18 ±0.28
Agarose (1.5%)		13.3	13.4	0.05	2.25 ±0.~~67~~[d]67[d]
PL161 (15%)	25	42.7	61.2	18.5	43.7 ± 5.50
	40	64.2	70.2	6.1	7.34 ± 0.35
DPPC:Ch	25	46.6	51.4	4.8	3.68 ± 1.1 [fe]
	40	31.2	39.0	7.8	10.85 ± 3.2 [f]

B_1 field (RMS) at ~~[a]~~4, ~~[b a]~~10.8 , and [e b]10.2 µT

[d c]T_{1D} as determined by fitting a single exponential decay to Jeener-Broekaert data. Errors are 95% confidence levels of fit.

[e d]10% agarose in D_2O (w/w).

[f e]Measured at 11.7 T. Other specimen and sample data collected at 2.0 T.

Figure Captions

Figure 1. Simulation of MT (blue), eMT (yellow) and ihMT (rust) spectra for T_{1D} = 2~~5~~0 ms (a) and ~~1.0~~200 ~~μ~~s (b) according to Provotorov formalism shown in Eqs. [1] and [2]. ihMT is large when T_{1D} is long and minimal when T_{1D} is short. An example of fitting Provotorov theory to ihMT data collected from a sample of Prolipid 161 (c). These simulations and fittings show ~~similar behavior to experimental results in Figs. 4 and 5~~that Provotorov theory helps explain the additional MT generated by dual-frequency RF saturation.

Figure 2. MT and eMT Pulse sequences for MRI and NMR studies. Bovine spinal cord imaging (a), single-shot MT and eMT for protonated samples (b), solid-state proton NMR with MT and eMT for deuterated samples (d), and proton T_{1D} measurement in deuterated samples (d). To eliminate multiple quantum and Zeeman order coherences in proton T_{1D} measurements, 8 step quadrature phase cycling was (e) $\phi1$= 00112233, $\phi2$ = 11221122, $\phi3$ = 02020202, and $\phi4$ = 20200202.

~~Figure 2. Percent ihMTR (a), MTR (b), and pixel histograms segmented by white matter and gray matter. ROC analysis reveals that ihMTR and MTR have similar sensitivity for white matter/gray matter segmentation but ihMTR has higher specificity. Colorbars represent percent ihMTR (a) or MTR (b).~~

Figure 3. Percent MTR (a,d), eMTR (b,e), and ihMTR (c,f) of formalin fixed bovine spinal cord (BSC) at 20 °C (a-c) and 40 °C (d-f). The amount of ihMTR in white matter (white arrow) changes significantly upon heating to 40 °C when compared to gray matter (black arrow). Grayscale images are %MTR and color images % ihMTR.

Figure 4. MT (solid blue), eMT (dashed yellow), and ihMT (solid rust) in gelatin (a), agarose (b) and Prolipid 161 (c). ihMT is effectively zero for gelatin and agarose and approximately 20% at 10 kHz in PL161. Lamellar lipid bilayers, such as in PL161 or in white matter, create structural and dynamic conditions favorable for generation of ihMT.

Figure 5. Illustration of amplitude and width of MT (a), eMT (b) and ihMT (c) profiles in 15% PL161 as function of temperature. Data were acquired from 5 to 85 °C as indicated in (b).

Figure 6. Solid-state ^{1}H NMR spectra of PL161 in D_2O with single-sided and double-sided RF saturation. Wideline NMR spectra (a) show asymmetric saturation of the PL161 semisolid line if RF is applied at +10 kHz (orange line and arrow, (+/+)) or at -10 kHz (purple line and arrow, (-/-)). Residual water protons (HOD) have significant MT whereas methyl protons (upfield, or right of HOD) do not participate in MT. Saturation at with both +10 kHz and -10 kHz RF (+/-) creates additional suppression of the semisolid line (dashed red in (a)) and additional MT to HOD (dashed red in (b)).

Figure 7. Asymmetric, offset-dependent RF saturation in PL161:D_2O (a,c) and LLC (b,d). These data are the difference between spectra with positive RF saturation (+/+) and negative RF saturation (-/-) as a function of RF frequency. Individual difference spectra are extracted in (c,d) at 5 frequencies (also indicated by colored lines on (a,b)).

Figure 8. Difference between positive (+/+) and negative (-/-) RF saturation in PL161 (a) and DPPC:Ch (b) at 25 °C versus 45 °C for PL161 and 25 °C versus 40 °C for DPPC:Cho.

Figure 9. Jeener-Broekert decay of dipolar order in cartilage (a), ~~white matter (a) and~~ PL161 (b), and white matter (c) ~~-~~at 25 °C (blue) and 40 °C (rust). A monoexponential relaxation function is fitted to the data to estimate T_{1D} at 25 °C ($T_{1D}^{25^\circ}$, blue text) and 40 °C ($T_{1D}^{40^\circ}$, rust text). These trends follow imaging and spectroscopy results seen in Figs. (3c and 3f) and Fig. 5c, respectively.

~~Supporting Figure S1. MT and eMT Pulse sequences for MRI and NMR studies. 3D human imaging in vivo (a), bovine spinal cord imaging (b), single-shot MT and eMT for protonated samples (c), solid-state proton NMR with MT and eMT for deuterated samples (d), and proton T_{1D} measurement in deuterated samples (e). To eliminate multiple quantum and Zeeman order coherences in proton T_{1D} measurements, 8-step quadrature phase cycling was (e) $\phi1 = 00112233$, $\phi2 = 11221122$, $\phi3 = 02020202$, and $\phi4 = 20200202$.~~

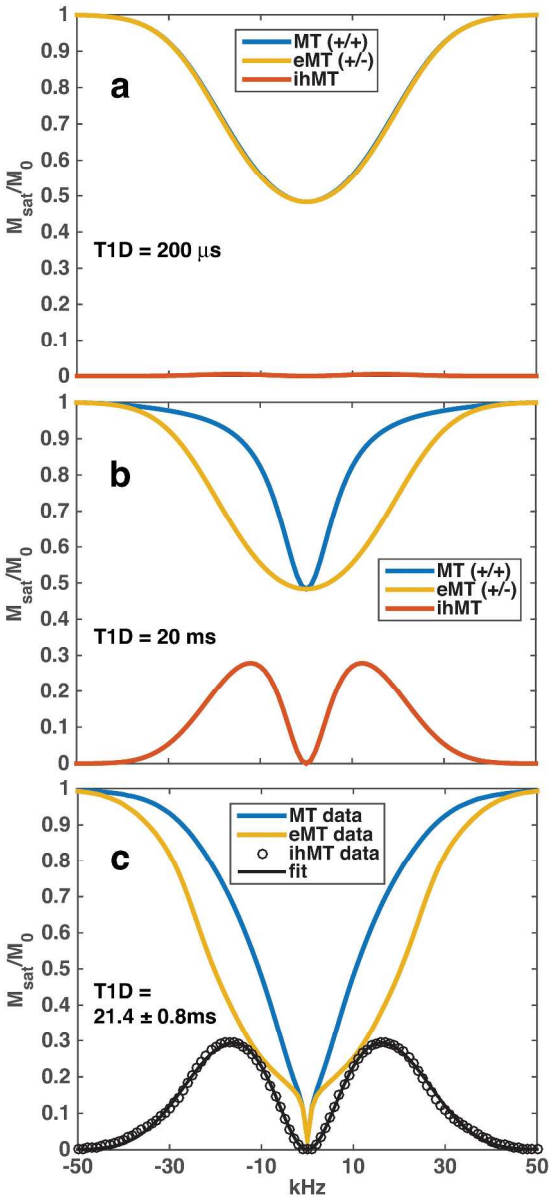

Figure 1. Simulation of MT (blue), eMT (yellow) and ihMT (rust) spectra for T_1D = 20 ms (a) and 200 μs (b) according to Provotorov formalism shown in Eqs. [1] and [2]. ihMT is large when T_1D is long and minimal when T_1D is short. An example of fitting Provotorov theory to ihMT data collected from a sample of Prolipid 161 (c). These simulations and fittings show that Provotorov theory helps explain the additional MT generated by dual-frequency RF saturation.
283x625mm (300 x 300 DPI)

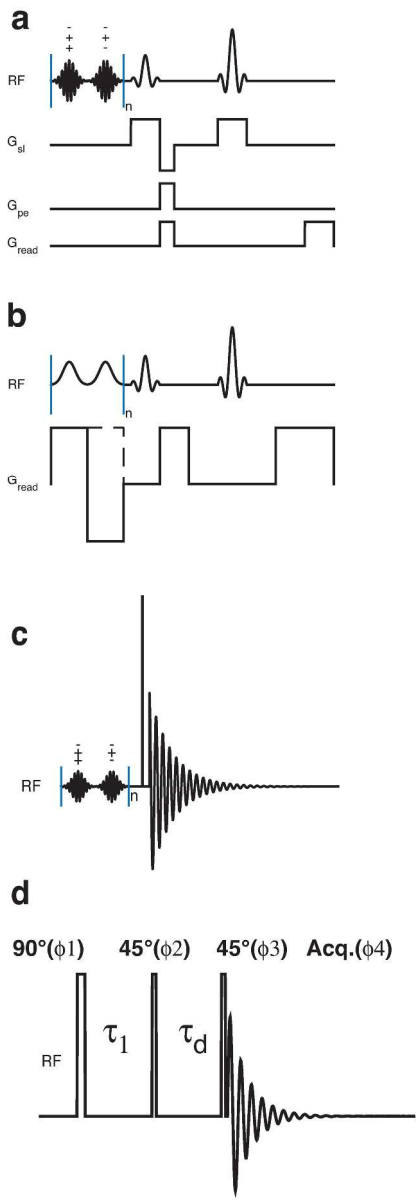

Figure 2. MT and eMT Pulse sequences for MRI and NMR studies. Bovine spinal cord imaging (a), single-shot MT and eMT for protonated samples (b), solid-state proton NMR with MT and eMT for deuterated samples (d), and proton T1D measurement in deuterated samples (d). To eliminate multiple quantum and Zeeman order coherences in proton T1D measurements, 8 step quadrature phase cycling was (e) ϕ1= 00112233, ϕ2 = 11221122, ϕ3 = 02020202, and ϕ4 = 20200202.
226x660mm (300 x 300 DPI)

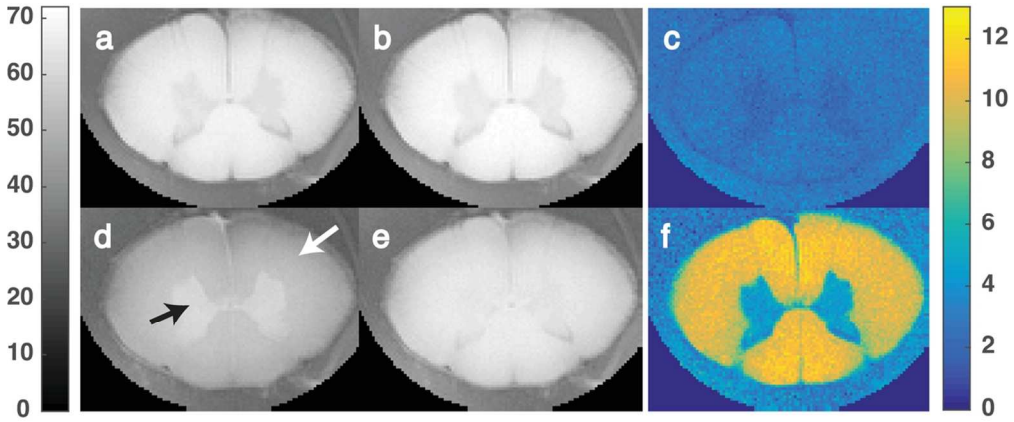

Figure 3. Percent MTR (a,d), eMTR (b,e), and ihMTR (c,f) of formalin fixed bovine spinal cord (BSC) at 20 °C (a-c) and 40 °C (d-f). The amount of ihMTR in white matter (white arrow) changes significantly upon heating to 40 °C when compared to gray matter (black arrow). Grayscale images are %MTR and color images % ihMTR.
111x47mm (300 x 300 DPI)

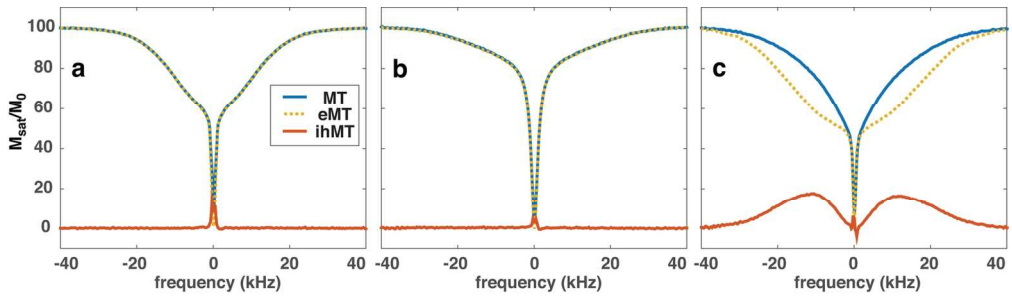

Figure 4. MT (solid blue), eMT (dashed yellow), and ihMT (solid rust) in gelatin (a), agarose (b) and Prolipid 161 (c). ihMT is effectively zero for gelatin and agarose and approximately 20% at 10 kHz in PL161. Lamellar lipid bilayers, such as in PL161 or in white matter, create structural and dynamic conditions favorable for generation of ihMT.
145x41mm (300 x 300 DPI)

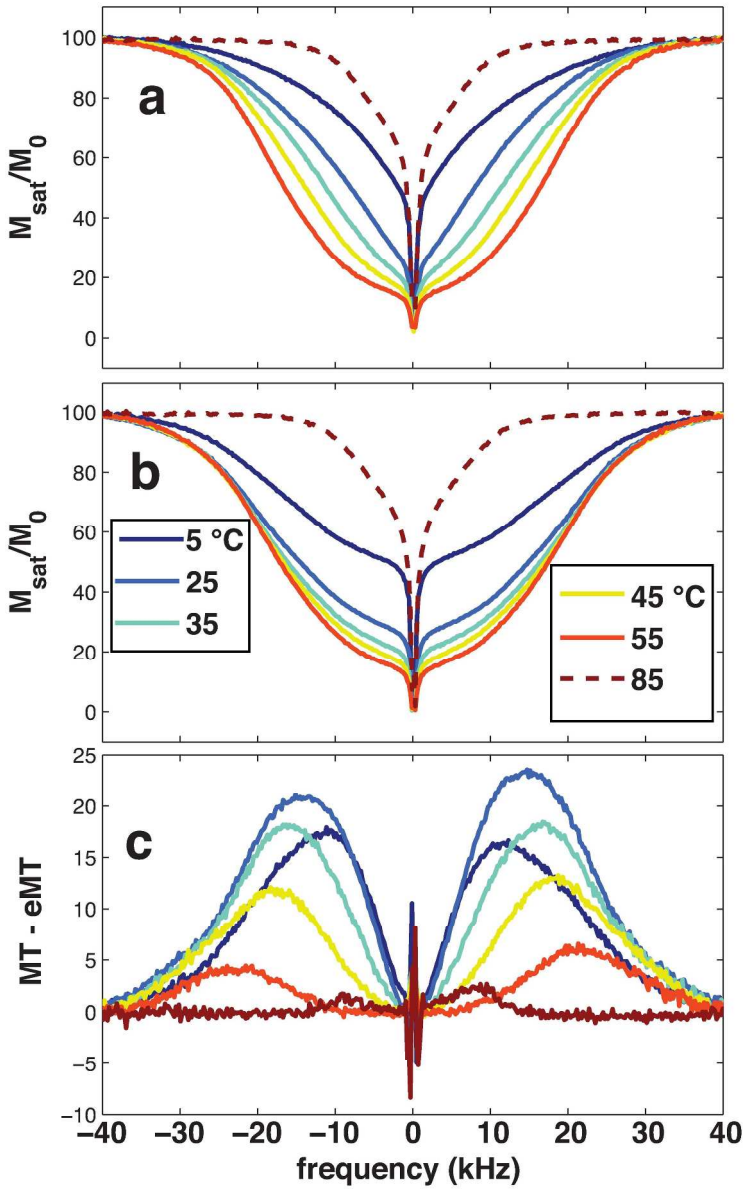

Figure 5. Illustration of amplitude and width of MT (a), eMT (b) and ihMT (c) profiles in 15% PL161 as function of temperature. Data were acquired from 5 to 85 °C as indicated in (b).
198x322mm (300 x 300 DPI)

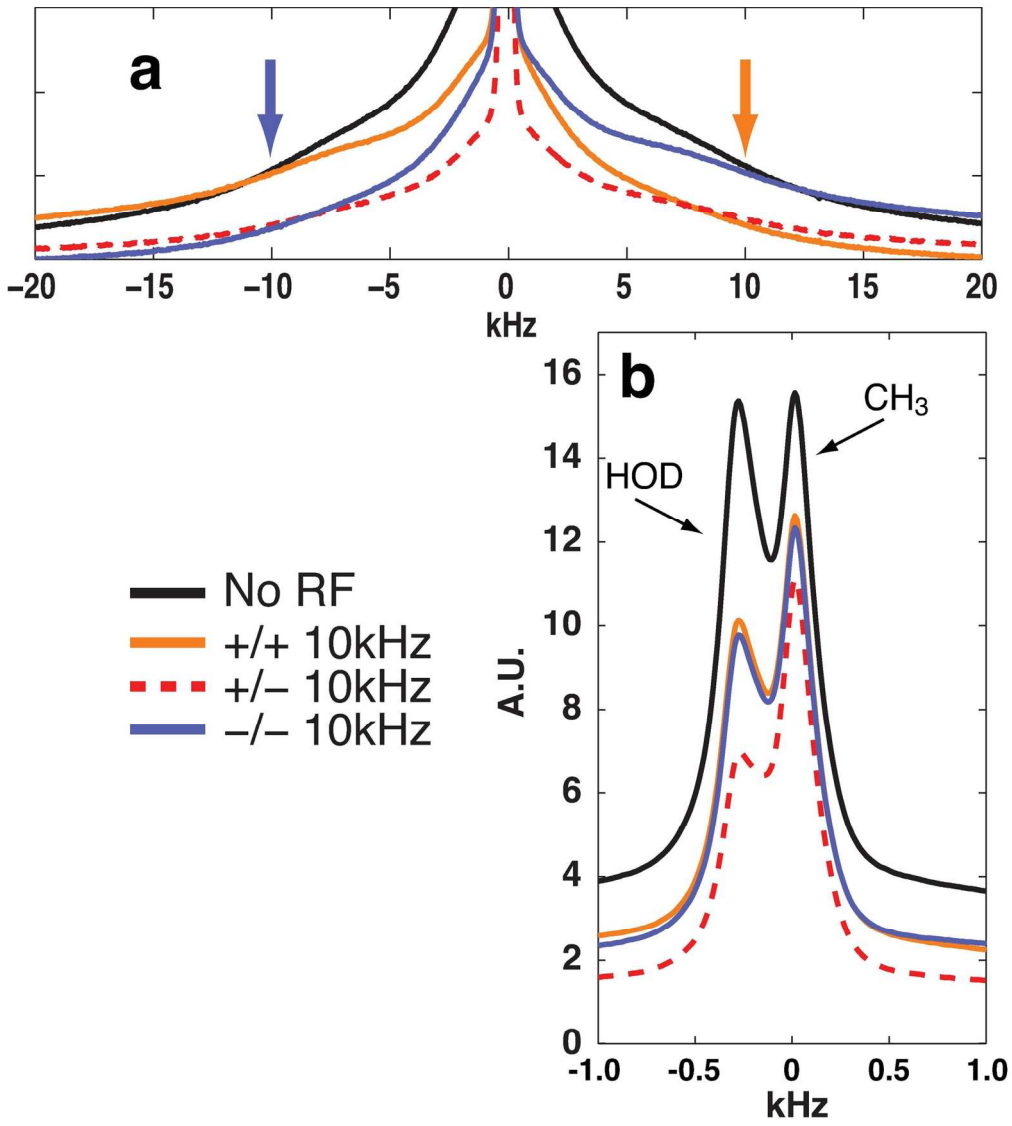

Figure 6. Solid-state 1H NMR spectra of PL161 in D2O with single-sided and double-sided RF saturation. Wideline NMR spectra (a) show asymmetric saturation of the PL161 semisolid line if RF is applied at +10 kHz (orange line and arrow, (+/+)) or at -10 kHz (purple line and arrow, (-/-)). Residual water protons (HOD) have significant MT whereas methyl protons (upfield, or right of HOD) do not participate in MT. Saturation at with both +10 kHz and -10 kHz RF (+/-) creates additional suppression of the semisolid line (dashed red in (a)) and additional MT to HOD (dashed red in (b)).
156x176mm (300 x 300 DPI)

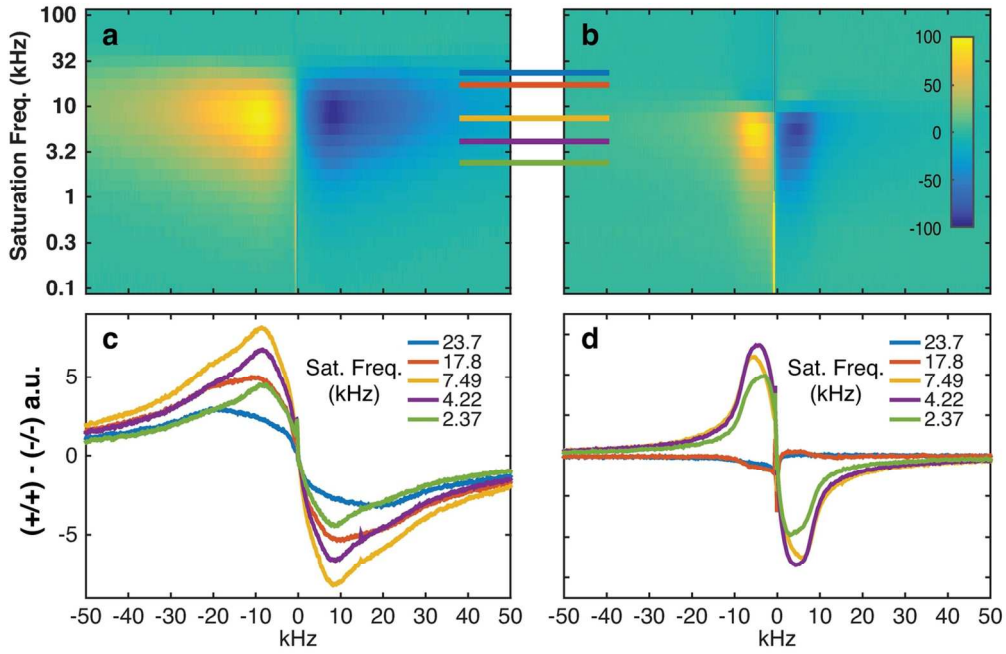

Figure 7. Asymmetric, offset-dependent RF saturation in PL161:D2O (a,c) and LLC (b,d). These data are the difference between spectra with positive RF saturation (+/+) and negative RF saturation (-/-) as a function of RF frequency. Individual difference spectra are extracted in (c,d) at 5 frequencies (also indicated by colored lines on (a,b)).
124x81mm (300 x 300 DPI)

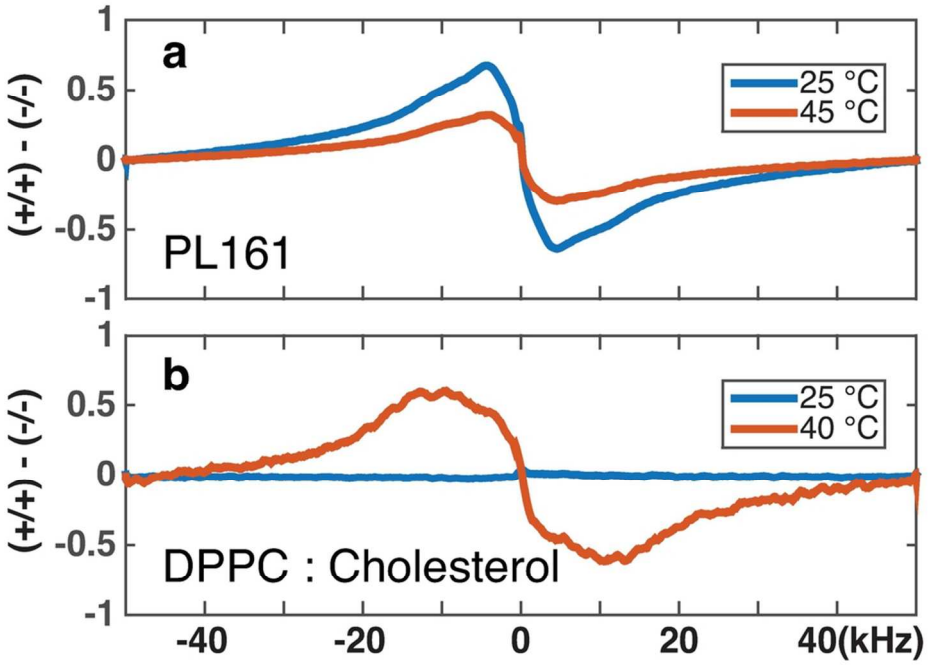

Figure 8. Difference between positive (+/+) and negative (-/-) RF saturation in PL161 (a) and DPPC:Ch (b) at 25 °C versus 45 °C for PL161 and 25 °C versus 40 °C for DPPC:Cho.
92x62mm (300 x 300 DPI)

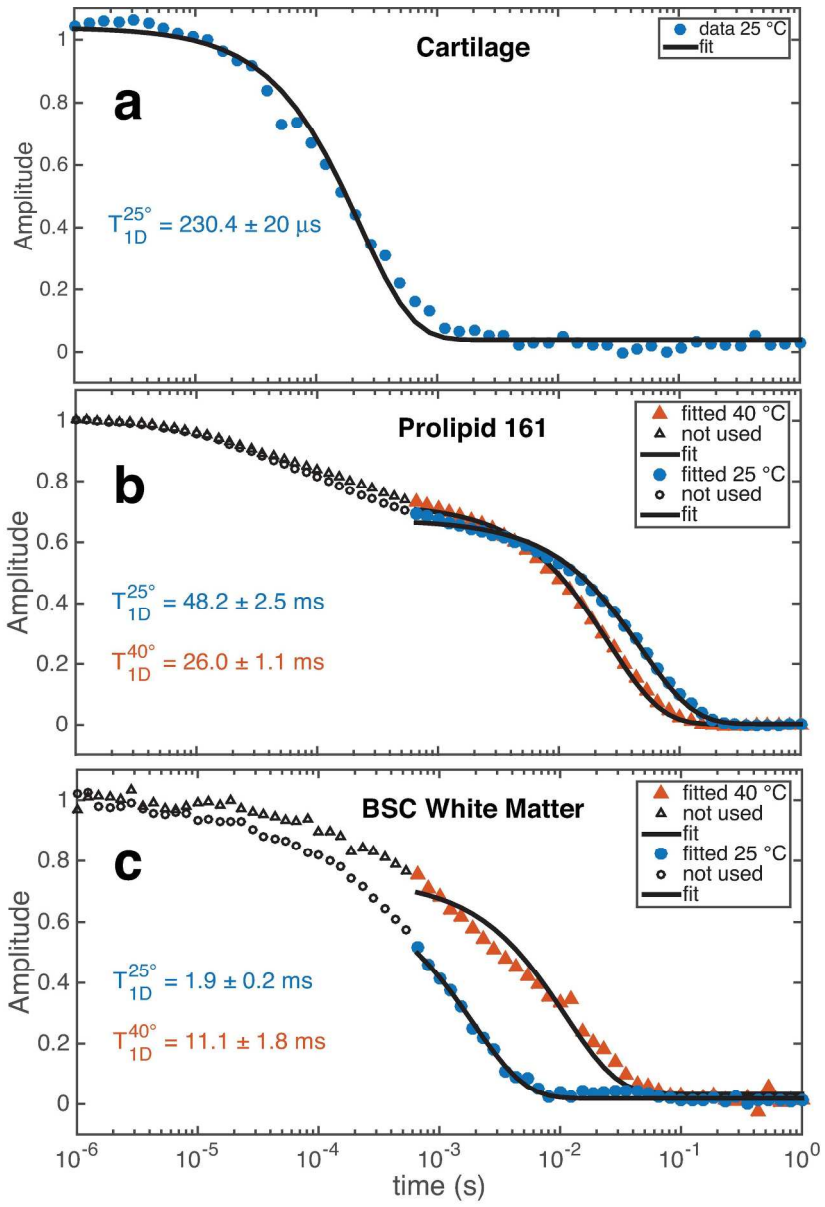

Figure 9. Jeener-Broekert decay of dipolar order in cartilage (a), PL161 (b), and white matter (c) at 25 °C (blue) and 40 °C (rust). A monoexponential relaxation function is fitted to the data to estimate T1D at 25 °C (T_1D^(25°), blue text) and 40 °C (T_1D^(40°) , rust text). These trends follow imaging and spectroscopy results seen in Figs. (3c and 3f) and Fig. 5c, respectively.
191x281mm (300 x 300 DPI)